Single-nuclear transcriptomics reveals diversity of proximal tubule cell states in a dynamic response to acute kidney injury

Louisa M. S. Gerhardt[a,1], Jing Liu[a,1], Kari Koppitch[a], Pietro E. Cippà[a,2], and Andrew P. McMahon[a,3]

[a]Department of Stem Cell Biology and Regenerative Medicine, Eli and Edythe Broad Center for Regenerative Medicine and Stem Cell Research, Keck School of Medicine of the University of Southern California, Los Angeles, CA 90033

This contribution is part of the special series of Inaugural Articles by members of the National Academy of Sciences elected in 2020.

Contributed by Andrew P. McMahon, April 23, 2021 (sent for review December 28, 2020; reviewed by Lloyd G. Cantley and Mark P. de Caestecker)

Acute kidney injury (AKI), commonly caused by ischemia, sepsis, or nephrotoxic insult, is associated with increased mortality and a heightened risk of chronic kidney disease (CKD). AKI results in the dysfunction or death of proximal tubule cells (PTCs), triggering a poorly understood autologous cellular repair program. Defective repair associates with a long-term transition to CKD. We performed a mild-to-moderate ischemia–reperfusion injury (IRI) to model injury responses reflective of kidney injury in a variety of clinical settings, including kidney transplant surgery. Single-nucleus RNA sequencing of genetically labeled injured PTCs at 7-d ("early") and 28-d ("late") time points post-IRI identified specific gene and pathway activity in the injury–repair transition. In particular, we identified *Vcam1*$^+$/*Ccl2*$^+$ PTCs at a late injury stage distinguished by marked activation of NF-κB–, TNF-, and AP-1–signaling pathways. This population of PTCs showed features of a senescence-associated secretory phenotype but did not exhibit G_2/M cell cycle arrest, distinct from other reports of maladaptive PTCs following kidney injury. Fate-mapping experiments identified spatially and temporally distinct origins for these cells. At the cortico-medullary boundary (CMB), where injury initiates, the majority of *Vcam1*$^+$/*Ccl2*$^+$ PTCs arose from early replicating PTCs. In contrast, in cortical regions, only a subset of *Vcam1*$^+$/*Ccl2*$^+$ PTCs could be traced to early repairing cells, suggesting late-arising sites of secondary PTC injury. Together, these data indicate even moderate IRI is associated with a lasting injury, which spreads from the CMB to cortical regions. Remaining failed-repair PTCs are likely triggers for chronic disease progression.

acute kidney injury | proximal tubule | repair | transcriptomics | single-nucleus RNA sequencing

Acute kidney injury (AKI) is a major global health problem with an annual incidence of ∼13.3 million cases worldwide (1). Major causes of AKI are ischemia–reperfusion injury (IRI) often related to surgical procedures, sepsis, and nephrotoxic drugs (2). AKI is associated with increased in-hospital mortality, longer hospital stays, and higher health care costs (3). Moreover, AKI can contribute to the development of chronic kidney disease (CKD), a condition currently affecting around 9.1% of the world's population and responsible for 1.2 million annual deaths (4). Analysis of kidney biopsies in kidney transplant patients has identified similar transcriptional and cellular signatures to those observed following severe IRI resulting in chronic disease progression, suggesting longer-term consequences for even moderate kidney injury (5–7). To date, there is no pharmacological strategy to treat AKI or prevent disease progression from AKI to CKD. A comprehensive understanding of the pathophysiologic mechanisms underlying AKI and driving the transition from AKI to CKD is therefore imperative.

Proximal tubule cells (PTCs) are the predominant cell type in the mammalian kidney. The epithelial proximal tubule is responsible for maintaining electrolyte balance and fluid homeostasis. PTCs exhibit high metabolic activity, are especially susceptible to ischemia, and play a critical role in the pathophysiology of CKD (2). In fact, in response to injury surviving PTCs can activate an intrinsic repair process, reenter mitosis, and regenerate the tubular epithelium restoring kidney architecture and function (8–11). However, renal repair is limited; even if renal function returns to baseline after an acute insult, residual inflammatory and fibrotic processes in the kidney can contribute to the development of CKD (2, 9, 12). Studies in animal models have linked disease progression to PTCs in G_2/M cell cycle arrest, which secrete proinflammatory and profibrotic cytokines (12, 13), but the underlying mechanisms driving the transition from AKI to CKD remain to be delineated.

Single-cell and single-nucleus mRNA sequencing (snRNA-seq) provides an unbiased approach to characterize transcriptional profiles associated with kidney injury and repair. Here, we employed genetic labeling strategies focused on PTCs to specifically study injured PTCs in a moderate IRI model using snRNA-seq. Lineage tracing experiments highlight a cell type with a proinflammatory, profibrotic, senescence-associated secretory phenotype, which originates from PTCs failing to repair at the primary injury site, and at cortical injury sites, likely arising from a spread of injury

Significance

A single acute kidney injury event increases the risk of progression to chronic kidney disease (CKD). Combining single-nucleus RNA sequencing with genetic tracing of injured proximal tubule cells identified a spatially dynamic, evolving injury response following ischemia–reperfusion injury. Failed proximal tubule repair leads to the persistence of a profibrotic, proinflammatory *Vcam1*$^+$/*Ccl2*$^+$ cell type exhibiting a senescence-associated secretory phenotype and a marked transcriptional activation of NF-κB and AP-1 pathway signatures, but no signs of G_2/M cell cycle arrest. Insights from this study can inform strategies to improve renal repair and prevent CKD progression.

Author contributions: L.M.S.G., J.L., K.K., P.E.C., and A.P.M. designed research; L.M.S.G., J.L., K.K., and P.E.C. performed research; L.M.S.G., J.L., P.E.C., and A.P.M. analyzed data; and L.M.S.G. and A.P.M. wrote the paper.

Reviewers: L.G.C., Yale University School of Medicine; and M.P.d.C., Vanderbilt University Medical Center.

Competing interest statement: A.P.M. is a scientific advisor on kidney-related approaches to human disease for Novartis, eGenesis, Iviva, and Trestle Biotherapeutics.

See QnAs, e2109575118, in vol. 118, issue 27.

[1]L.M.S.G. and J.L. contributed equally to this work.

[2]Present address: Division of Nephrology, Ente Ospedaliero Cantonale, 6500 Lugano, Switzerland.

[3]To whom correspondence may be addressed. Email: amcmahon@med.usc.edu.

This article contains supporting information online at https://www.pnas.org/lookup/suppl/doi:10.1073/pnas.2026684118/-/DCSupplemental.

Published June 28, 2021.

following the primary IRI event. These data highlight a dynamic injury response identifying cell types, cell pathways, and molecular targets for therapeutic evaluation in the transition of AKI to CKD.

Results and Discussion

In a previous study of the progression from AKI to CKD in a long-term bilateral IRI model, we identified keratin-20 (Krt20) as a marker of injured PTCs (5). To enable the isolation and tracing of Krt20$^+$ cells in renal injury, we generated a *Krt20*$^{T2A\text{-}CE}$ mouse line through homology-directed repair (HDR) following CRISPR-Cas9-cleavage of *Krt20* in mouse embryo stem cells and the production of germline chimeras (Fig. 1*A*). HDR results in the production of a CRE-ERT2 (CE) fusion protein in *Krt20*-expressing cells through the insertion of a T2A self-cleaving peptide at the carboxyl terminus of *Krt20*. Crossing *Krt20*$^{T2A\text{-}CE}$ to *Gt(ROSA)26Sor*$^{tm5(CAG\text{-}Sun1/sfGFP)Nat}$ mice, which express green fluorescent protein (GFP) linked to a nuclear membrane protein in the presence of Cre and are further referred to as INTACT (Isolation of Nuclei TAgged in specific Cell Types) mice (14, 15), enabled tamoxifen-dependent labeling of nuclei in injured PTCs.

To model moderate kidney injury as may occur in a variety of non–life-threatening clinical settings such as in the course of kidney transplant surgery, we assayed different ischemia intervals. In double transgenic male mice, an 18-min ischemia interval resulted in a small but significant increase (twofold to threefold) in basal creatinine and blood urea nitrogen (BUN) levels 48 h post-IRI (*SI Appendix*, Fig. S1 *A* and *B*). Creatinine and BUN levels were restored to baseline by 28 d post-IRI. Double transgenic mice subjected to IRI were injected with tamoxifen on days 5 and 6, or days 26 and 27 post-IRI, and kidneys collected at day 7 (designated "early"; $n = 2$) or day 28 (designated "late"; $n = 3$) post-IRI, respectively (Fig. 1*B*). For snRNA-seq, GFP$^+$ nuclei were isolated using fluorescence-activated cell sorting (FACS) and snRNA-seq profiles identified through 10× Genomics profiling and NextGen sequencing. As a control dataset, we combined our published snRNA-seq data of FACS-sorted GFP$^+$ nuclei where a GFP linked to the histone protein H2B is present in all nephron cells (16), with additional replicate data from this line (one non-surgery and three sham-operated control mice).

Immunofluorescence studies confirmed successful labeling of *Krt20*-expressing cells with a labeling efficiency of around 34% (Fig. 1 *C* and *F*). The labeling efficiency was consistent in comparisons of data at day 7 and day 28 post-IRI. Most labeled cells were positive for the proximal tubule injury marker Havcr1 (Fig. 1*F* and *SI Appendix*, Fig. S1*E*) (17). While the total number of labeled *Krt20*-expressing PTCs decreased from day 7 to day 28 post-IRI, the predominant location of these cells shifted from the cortico-medullary boundary (CMB) (zone highlighted in *SI Appendix*, Fig. S1*C*) in early injured samples to the outer cortex at 28 d (Fig. 1 *D* and *E* and *SI Appendix*, Fig. S1 *D* and *F*).

IRI and control snRNA-seq datasets were integrated using the Seurat R package (18), low-quality profiles filtered from the main dataset, and 24,086 nuclear profiles analyzed by unsupervised clustering. The resulting 13 distinct clusters are presented as two-dimensional uniform manifold approximation and projection (UMAP) plot (Fig. 1*G*). Differential gene expression analysis identified cluster-specific marker genes and the clusters were annotated using known marker genes of kidney cell types, immune cells, vasculature, and interstitial cells (Fig. 1*H* and *SI Appendix*, Fig. S2*B*). As expected, our datasets strongly enriched for proximal tubule nuclei in both the control and IRI treatments. Small clusters of non-PTC signatures in the control and IRI datasets most likely represent a relatively lenient selection of GFP$^+$ cells during FACS sorting. Using known marker genes, we unambiguously identified three dominant clusters as proximal tubule segments. Two other closely related clusters showed strong expression of the proximal tubule-specific injury marker *Havcr1* and were identified as injured PTCs (17). One of these injured proximal tubule clusters was distinguished by enriched expression of cell cycle genes, indicating a cycling state. The injured PTC clusters as well as the immune cell cluster were almost exclusively derived from the IRI replicates (*SI Appendix*, Fig. S2*A*).

For in-depth characterization of different PTC states, we performed a reclustering analysis of all PTCs (marked in Fig. 1*G*), which resolved 12 clusters. Data are presented as UMAP plot and tabulated lists of the most differentially expressed genes (Fig. 2*A* and Dataset S1). Both control and IRI replicates were represented together in 7 of the 12 clusters (0, 2, 3, 6, 7, 8, 9), while the other 5 clusters were mostly composed of IRI replicates, further referred to as IRI clusters (1, 4, 5, 10, 11) (Fig. 2*C*). Clustering of variable genes into modules of coregulated genes showed a clear distinction in the transcriptional profile between these two groups of clusters (*SI Appendix*, Fig. S3). Clusters composed of both control and IRI replicates showed higher expression of *Hnf4a*, a key transcription factor governing proximal tubule differentiation, and its target gene *Lrp2*, than clusters predominantly derived from IRI samples (Fig. 2*B*) (19, 20). This is in line with the previously described down-regulation of the normal proximal tubule transcriptional signature upon injury (5, 21, 22). Clusters expressing *Lrp2* were further subdivided into distinct proximal tubule segments through segment-specific markers such as *Slc5a12* (S1), *Slco1a1* (S2), and *Slc7a13* (S3) (Fig. 2*B*).

Interestingly, several clusters displayed normal S1, S2, and S3 signatures, but enrichment of different proximal tubule marker genes indicating heterogeneity among the PTCs. The S3 cluster 8, for example, showed ectopic activation of *Slc7a12*, a female-specific S3-marker gene, in IRI replicates (23), while also showing expected expression of characteristic male S3 segment-specific genes like *Cyp7b1* (Fig. 2*B*). The predicted up-regulation of *Slc7a12* in male PTCs after IRI was confirmed by RNAscope in situ hybridization studies (Fig. 3*A*). Some *Slc7a12*$^+$ PTCs were positive for *Slc22a7*, a marker of both female and male proximal tubule segment S3, while others showed coexpression of the vascular cell adhesion molecule-1 (Vcam1), a known marker of inflammatory renal diseases and AKI (21, 24). These data indicate *Slc7a12* expression is up-regulated in injured Vcam1$^+$, *Slc22a7*$^-$ PTCs, and suggest that *Slc7a12* expression may persist in PTCs that recovered, regaining *Slc22a7* and losing Vcam1. Alternatively, *Slc7a12* may also be ectopically activated in *Slc22a7*$^+$ cells without a strong injury signature. Analysis of a published snRNA-seq dataset of male kidneys 14 d after unilateral ureteral obstruction through a searchable database (humphreyslab.com/SingleCell/) also showed enriched *Slc7a12* expression in PTCs (25). Thus, the activation of a female-like *Slc7a12* expression pattern in the male kidney on AKI is not confined to the IRI model.

Gene ontology (GO) term analysis of the differentially expressed genes in each proximal tubule cluster showed enrichment of terms related to normal proximal tubule structure and function in the S1 and S2/3 clusters across all GO categories. For example, in the category biological process, the terms "organic anion transport" and "drug transport" were enriched, while in the category cellular component, the terms "brush border membrane" and "apical part of cell" were overrepresented (Fig. 2 *D* and *F* and Dataset S2). Interestingly, the S1 cluster 7 and the S2/3 cluster 3 showed enrichment of "respiratory chain," "mitochondrial inner membrane," and "cytochrome *c* oxidase activity" (Dataset S2), possibly indicating increased energy demand in these cells. *Spag5*, encoding a mitotic spindle protein shown to be up-regulated in response to oxidative stress in cancer (26) and in response to high glucose treatment in human podocytes (27), was overrepresented in these clusters as well as in cluster 8 (Fig. 2*B*).

Among the IRI clusters we identified two "early injured," two "early + late injured," and one "late injured" cluster based on the predominant composition of clusters by IRI replicates (Fig. 2 *B* and *C*). The early injured clusters showed enriched expression of *Havcr1* and the cadherin encoding genes *Cdh6* and

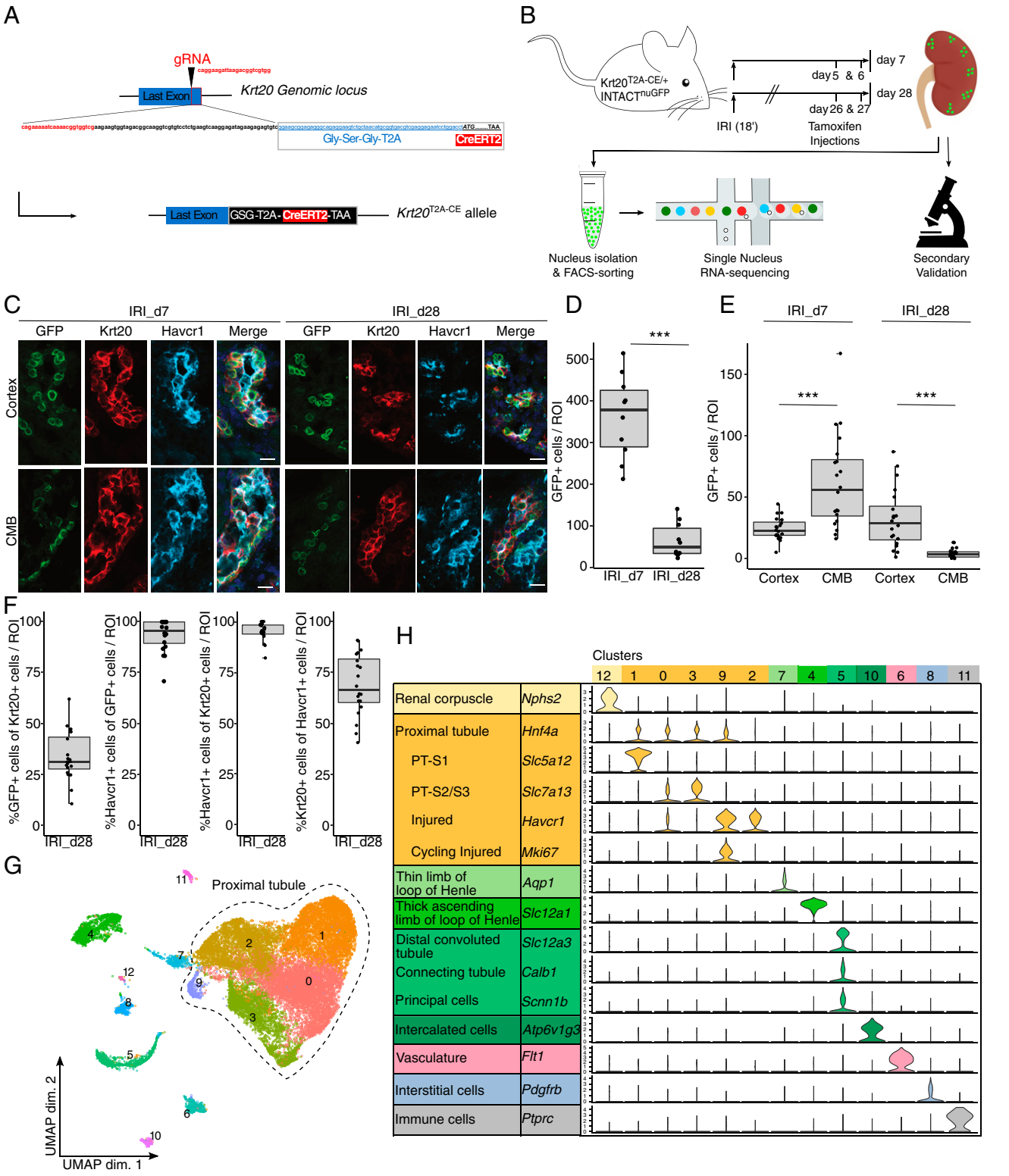

Fig. 1. *Krt20* inducible Cre-LoxP system traces injured PTCs in post-IRI kidneys. (*A*) Schematic diagram of CRE-ERT2 (CE) knocked into *Krt20* genomic locus through CRISPR. (*B*) Experimental setup. (*C*) Colocalization of GFP reporter with Krt20 and Havcr1 on IRI samples. (Scale bar, 20 μm.) (*D*) Quantification of GFP$^+$ cells per region of interest (ROI) using five ROIs per kidney section ($n = 2$). (*E*) Quantification of GFP$^+$ cells per ROI in cortex and cortico-medullary boundary (CMB) using 10 cortical and CMB ROIs per kidney section ($n = 2$). (*F*) Quantification of colocalization of GFP reporter, Krt20, and Havcr1 per ROI, 10 ROIs per kidney section ($n = 2$). (*G*) UMAP plot of the integrated IRI and control single-nuclei RNA-sequencing datasets. (*H*) Violin plots of marker genes arranged by cell type; cluster numbers are indicated above the plots. In *D*–*F*, the gray box corresponds to the middle 50th percentile, the horizontal line to the median, and the whiskers indicate the 1.5 interquartile range. ***$P < 0.001$.

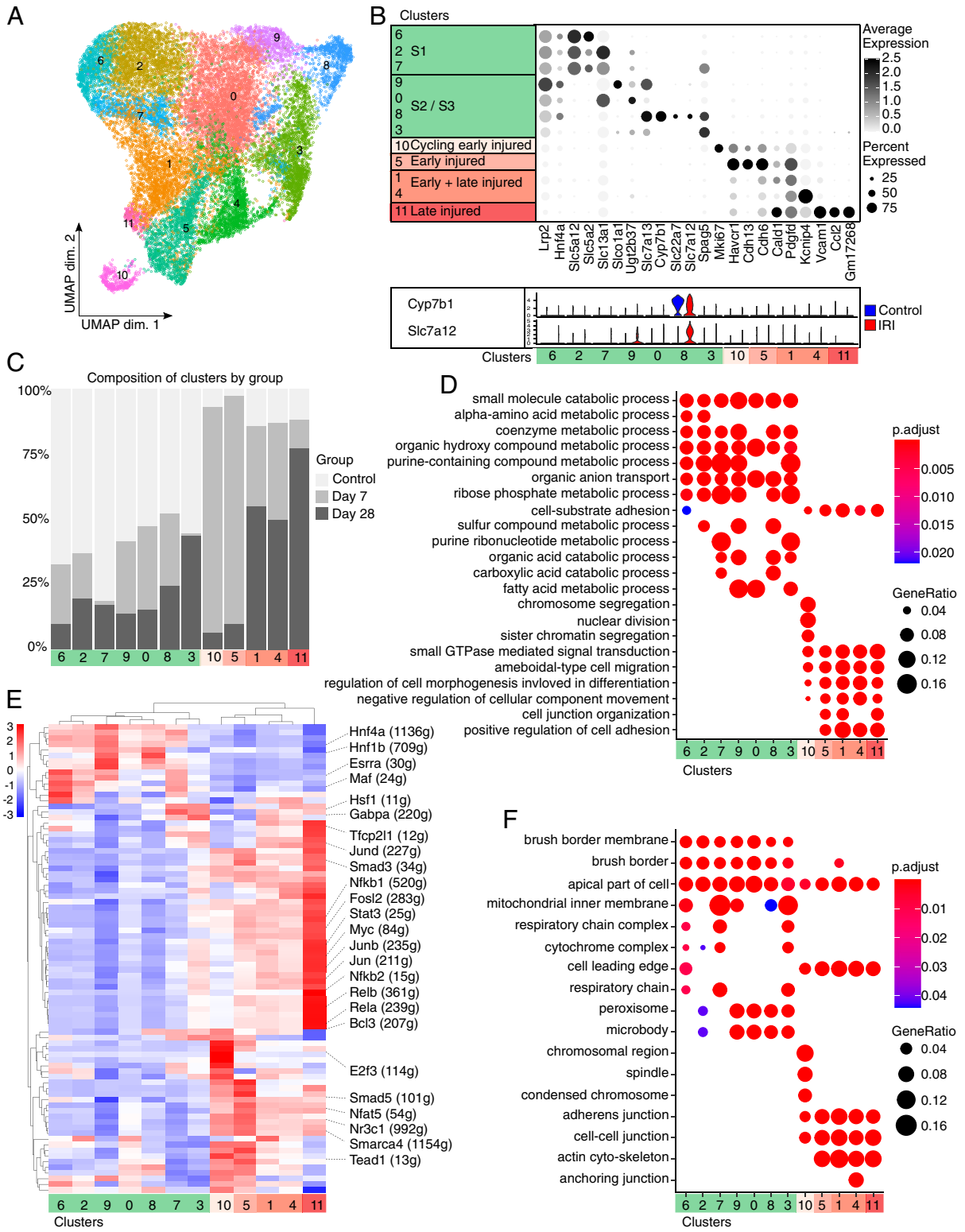

Fig. 2. PTCs adopt transcriptionally diverse cell states in response to injury. (*A*) UMAP plot of the PTC clustering. (*B*) Dot plot of cluster enriched gene expression. Violin plot of male-specific S3 segment marker *Cyp7b1* and female-specific S3 segment marker *Slc7a12* across clusters split in IRI and control cells. (*C*) Stacked bar plot of the composition of clusters by group. (*D*) GO analysis of biological processes and cellular components (*F*) across clusters. Top three enriched GO terms per cluster are shown. (*E*) Gene-regulatory network analysis using single-cell regulatory network inference and clustering (SCENIC) across IRI cells. Heatmap showing regulon activity across clusters. Transcription factors representative for each group are highlighted. See Dataset S3 for a complete list of identified regulons.

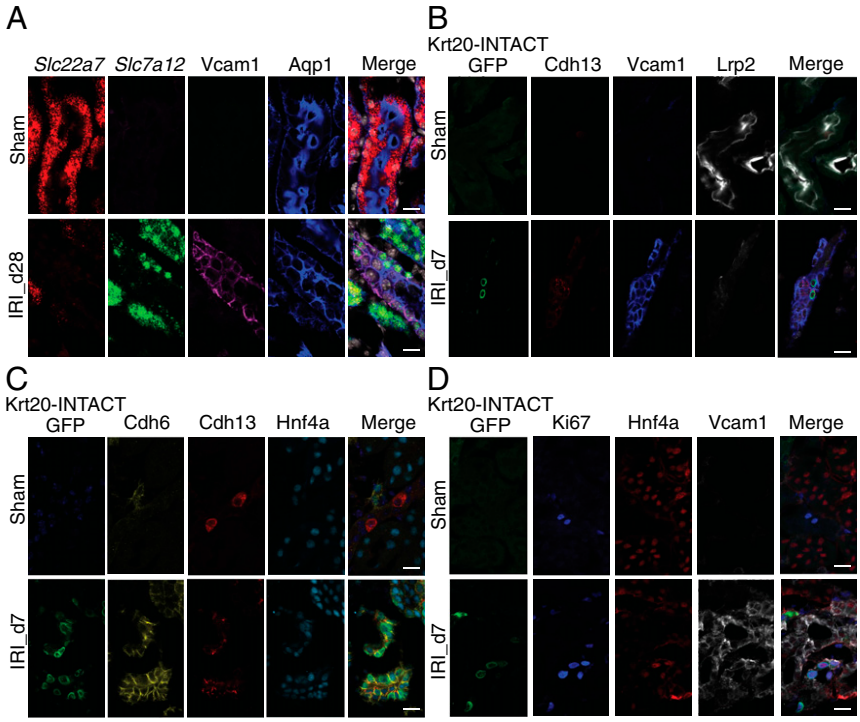

Fig. 3. Validation of identified injured PTC states. (*A*) A combination of RNAscope (*Slc22a7* and *Slc7a12*) and immunofluorescence (Vcam1 and Aqp1) in the same sections shows up-regulation of female-specific gene *Slc7a12* in male mice after IRI. (*B–D*) Immunofluorescence staining of Cdh6, Cdh13, Ki67, Vcam1, Hnf4a, and Lrp2 in proximal tubules validates identified PTC states. (Scale bar: *A–D*, 20 μm.)

Cdh13. In the normal kidney, *Cdh6* and *Cdh13* demarcate cells making up the descending thin limb of the inner stripe of the outer medulla for cortical and juxtamedullary nephrons, respectively (https://cello.shinyapps.io/kidneycellexplorer/) (23). Immunofluorescence studies confirmed the de novo up-regulation of Cdh6 and Cdh13 in injured PTCs (Fig. 3 *B* and *C*). The early injured cluster 10 was distinguished by high expression of genes involved in DNA replication such as *Mki67* and *Top2a*, indicative of a cycling cell state (Figs. 2*B* and 3*D*). The restriction of a strong replicative response to early injury clusters is in line with the injury-invoked replicative repair.

Early and late injured clusters 1 and 4 were characterized by enriched expression of *Cald1* and *Pdgfd*, while *Kcnip4* was markedly up-regulated in cluster 4 specifically. *Cald1* encodes Caldesmon 1, an actin-linked regulatory protein of the smooth muscle and nonmuscle contractile apparatus that is expressed in fibroblasts in the healthy kidney and has been associated with diabetic nephropathy (28, 29). The platelet-derived growth factor D (*Pdgfd*) is known to play a role in renal fibrosis (30), and *Kcnip4*, encoding potassium channel-interacting protein 4, has recently been described to be up-regulated in a distinct proinflammatory, profibrotic PTC state that persists weeks after AKI (21). Consistent with this finding, *Kcnip4* was expressed in the late injured cluster 11 although at lower levels than in cluster 4. Cluster 11 was distinguished from other clusters by strong expression of *Vcam1* and the monocyte chemoattractant protein-1 encoding gene *Ccl2*. *Ccl2* is tightly linked on mouse chromosome 11 with *Ccl7* and the predicted protein coding gene model *Gm17268*. All three transcripts were among the most specific markers of the cluster 11 late injury cell population (Dataset S1). The presence of $Ccl2^{+}$, $Vcam1^{+}$, $Krt20^{+}$ cells in the injured kidney 4 wk after AKI was validated by immunofluorescence and RNAscope studies (see Fig. 5 *A* and *B* and *SI Appendix*, Fig. S4*C*).

GO term analysis indicated a clear functional distinction between normal S1, S2/S3, and IRI clusters (Fig. 2 *D* and *F* and Dataset S2). None of the terms related to normal proximal tubule structure and function were enriched in the IRI clusters, while new terms associated with changes in epithelial state, dedifferentiation, migration, and fibrosis were overrepresented (Fig. 2*D*). Furthermore, cellular components known to play a role in cell adhesion and migration like "actin cytoskeleton" and "adherens junction" were enriched in the IRI clusters (Fig. 2*F* and Dataset S2). The early proliferating cluster showed very cluster-specific enrichment of cell cycle related GO terms, underlining the confinement of a cycling cell state to the cells in this cluster (Fig. 2*D* and Dataset S2).

To obtain further insight into the regulatory states of cells in each cluster, we used single-cell regulatory network inference and clustering (SCENIC) to reconstruct gene-regulatory networks (Fig. 2*E* and Dataset S3) (31). S1, S2, and S3 showed activity of regulons involved in proximal tubule development, including *Hnf4a*, *Hnf1b*, and *Esrra* (19, 20, 32). Activity of these regulons associated with core PTC function was predicted to be down-regulated in the IRI clusters, which is in line with the marked loss of normal PTC gene expression profiles. Interestingly, two of the PTC clusters annotated as S1 and S3, cluster 7 and cluster 3, showed predicted regulon activity of *Hsf1*, encoding a master transcriptional regulator of heat shock proteins involved in stress and cancer (33) and *Hcfc1* (host cell factor C1), a transcriptional regulator that targets cell cycle genes depending on Hsp90 for its stability (34). In addition, cluster 3 shared activity of some regulons with IRI clusters. Clusters 3 and 7 likely represent PTCs with reduced PTC functions, reflected by reduced *Hnf4a* activity, and a stressed transcriptional state.

Proliferating early injured cells displayed *E2f3* regulon activity consistent with the replicating state of these cells. Gene-regulatory network analysis further suggested involvement of the Hippo signaling pathway in early injured cells: up-regulation of the *Tead1* regulon, a nuclear effector in an inactive Hippo signaling state associated with cell proliferation. The Hippo signaling pathway is

known to respond to altered tension and mechanical constraints in epithelial tissues (35), regulating organ development and growth through the control of cell proliferation and apoptosis. YAP and TAZ, key transcriptional coactivators acting together with Tead DNA binding partners, have been shown to play a role in cystic kidney disease progression and development of renal fibrosis following AKI (36). Consistent with Hippo engagement in early injured cells, differential gene expression analysis showed up-regulation of regulators involved in YAP-inactivation and Hippo signaling (e.g., *Sav1*, *Stk3*), as well as effectors of the transcriptional response when Hippo signaling is silenced (e.g., *Yap1*, *Tead1*) (37) and well-known YAP-target genes such as *Axl* and *Ctgf*. SCENIC also predicted IRI cluster-specific regulon activity of *Nfat5*, a transcription factor mediating cellular responses to hypertonic stress and hypoxia that has been described to diminish renal injury following IRI by reducing caspase-3–dependent apoptosis (38). *Nfat5* expression was enriched in all IRI clusters (Dataset S1).

Late injured cells of cluster 11 showed strongly up-regulated activity of regulons related to the NF-κB (*Nfkb1*, *Nfkb2*, *Rela*, *Relb*, *Bcl3*) and activator protein-1 (AP-1; *Jun*, *Junb*, *Jund*, and *Fosl2*) signaling pathways. Similar gene-regulatory networks have been described in many human cancers and provide further evidence for a proinflammatory state of these cells (39). In addition, activity of the *Smad3* regulon, an intracellular signal transducer activated by transforming growth factor-β (TGF-β), suggests these PTCs may also respond to TGF-β signaling that is linked to driving renal fibrosis in mesangial cells and adjacent stromal cell types

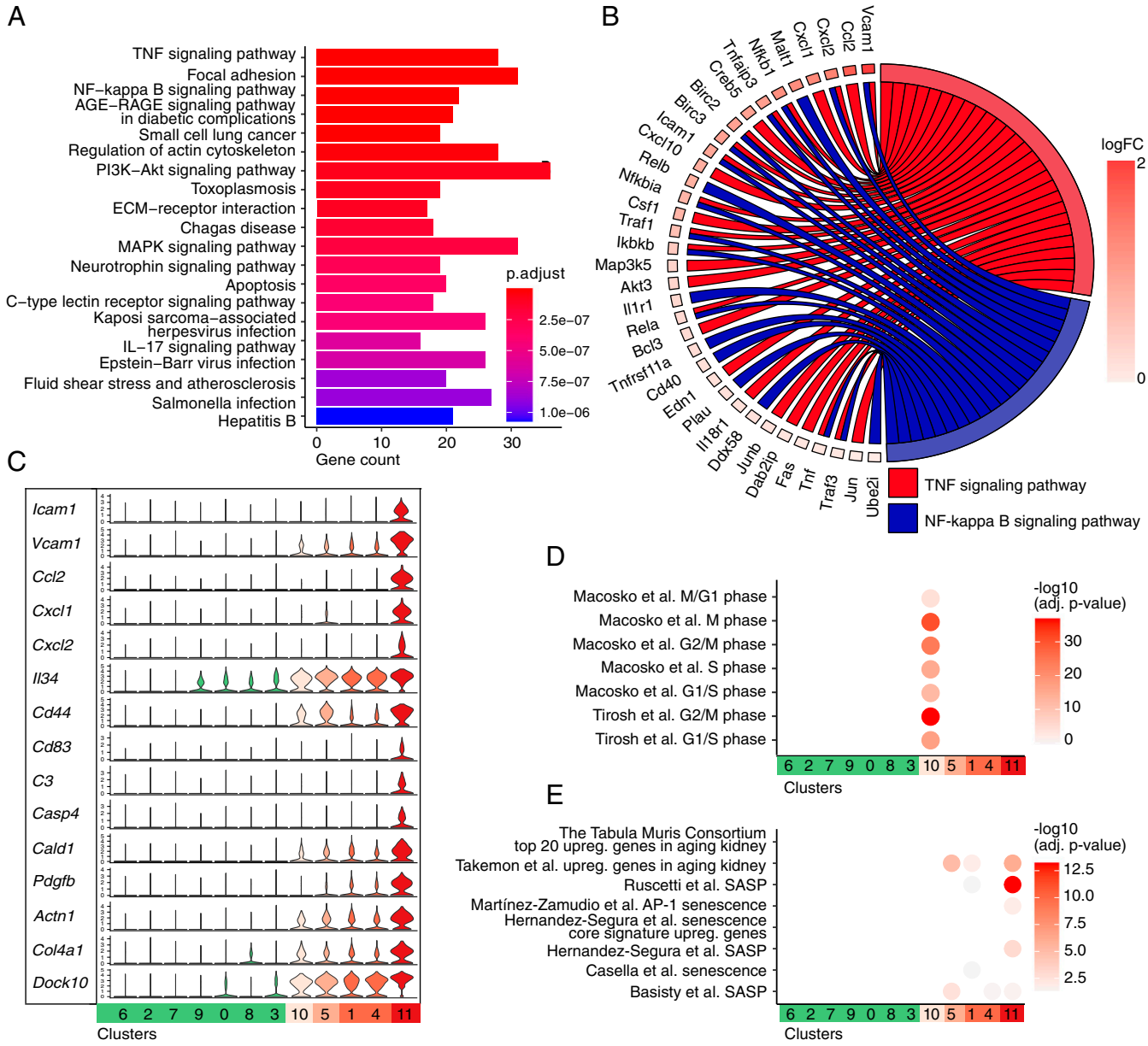

Fig. 4. *Vcam1*$^{+}$/*Ccl2*$^{+}$ proximal tubule subpopulation shows proinflammatory and profibrotic signature, but no G_2/M cell cycle arrest. (*A*) Top 20 enriched KEGG pathways in late injured cluster 11. (*B*) Depiction of the KEGG pathways TNF and NF-κB signaling with the involved genes up-regulated in cluster 11. (*C*) Violin plots displaying expression of selected features across proximal tubule clusters. The cluster numbers correspond to Fig. 2*A*. (*D*) Gene set enrichment analysis of published cell cycle and (*E*) senescence/senescence-associated secretory phenotype (SASP) gene sets across clusters. See Dataset S4 for details on used gene sets.

(40, 41). IRI clusters also displayed regulon activity of *Myc*, encoding the proto-oncogene c-Myc, which has been implicated in tubular cell apoptosis, and *Tfcp2l1*, which is associated with renal tubule development (42, 43).

Given the presence of the late injury cluster 11 in the kidney after normalization of kidney function, and an AKI linkage to development of CKD (9), we focused further analysis on this cluster. The most strongly enriched GO term in cluster 11 was "small GTPase mediated signal transduction," and dedicator of cytokinesis protein 10 (*Dock10*), a guanine nucleotide exchange factor that can activate Rho GTPases, was among the most up-regulated genes in cluster 11 (Fig. 4*C* and *SI Appendix*, Fig. S4*A*). *Dock10* has been described to be necessary for GTPase activation in amoeboid invasion of melanoma cells (44). Interestingly, GO terms like "ameboidal-type cell migration" and "epithelium migration" were also enriched in late injured cluster 11 cells, suggesting a migratory phenotype of these cells (*SI Appendix*, Fig. S4*A*).

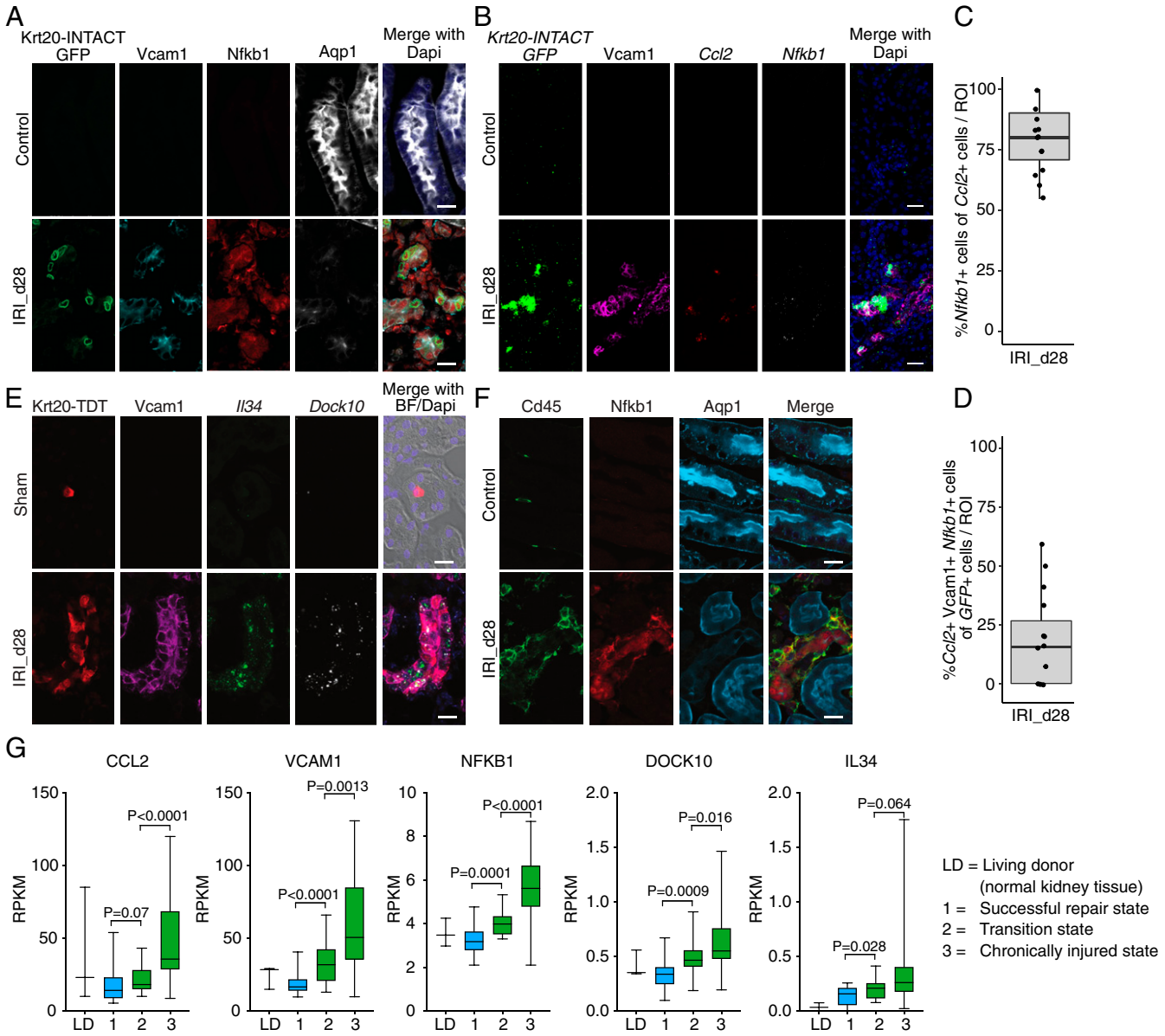

Fig. 5. Immunofluorescence and RNAscope validate *Nfkb1* expression in Vcam1^{+}/*Ccl2*$^{+}$ PTCs. (*A*) Immunofluorescence staining validates Nfkb1 and Vcam1 in Krt20^{+} cells. (*B*) Combination of RNAscope in situ hybridization (*Nfkb1*, *Ccl2*, *GFP)* and immunofluorescence staining (Vcam1) shows *Nfkb1*, *Ccl2*, Vcam1, and *Krt20-INTACT GFP*-coexpressing cells. (*C* and *D*) Quantification of (*C*) colocalization of *Nfkb1* with *Ccl2* in PTCs and of (*D*) *Ccl2*, Vcam1 and *Nfkb1* in *GFP*$^{+}$ PTCs using five regions of interest (ROIs) per kidney section ($n = 3$). The gray box corresponds to the middle 50th percentile, the horizontal line to the median, and the whiskers indicate the 1.5 interquartile range. (*E*) Combination of RNAscope in situ hybridization (*Il34*, *Dock10*) and immunofluorescence staining (Vcam1, Krt20-TDT) shows *Il34* and *Dock10* expression in Vcam1^{+}, Krt20^{+} cells marked by the fluorescent reporter tandem tomato (TDT) in *Krt20*$^{T2A\text{-}CE/+}$;*R26R*$^{tdTomato/+}$ mice. (*F*) Immunofluorescence staining shows Cd45^{+}, Nfkb1^{+} inflammatory cells around the Nfkb1^{+} tubules. See *SI Appendix*, Fig. S4*E* for validation of Nfkb1 antibody. (*G*) Box plots of reads per kilobase per million mapped reads (RPKM) values of indicated genes in bulk RNA-seq analysis of human kidney transplants biopsies in a successfully repaired [1] or a transition state [2] toward a chronically injured state [3]. Biopsy samples from living donors (LDs) were included as a representation of normal kidney tissue. Groups were compared by Mann–Whitney *U* test. Box corresponds to the middle 50th percentile, the horizontal line to the median, and the whiskers indicate the data range. Data adopted from ref. 7. (Scale bar: *A*, *B*, *E*, *F*, 20 μm.)

Kyoto Encyclopedia of Genes and Genomes (KEGG) pathway analysis indicated a strong up-regulation of TNF and NF-κB signaling: The NF-κB pathway is the primary mediator of TNF signaling (45) and AGE (advanced glycation end-product)/RAGE (AGE receptor) signaling, which has been linked to diabetic nephropathy (Fig. 4 *A* and *B*) (46). Differential gene expression analysis revealed up-regulation of the NF-κB complex (*Nfkb1*, *Relb*, *Rela*) as well as of potential activators/mediators (*Tnfα*, *Il-1r*, *Cd40*, *Rank*), regulators (*Malt1*), and target genes of the NF-κB signaling pathway (Fig. 4 *B* and *C*). Several of the up-regulated NF-κB target genes have been described to play a role in kidney disease: Il34 has been shown to promote macrophage proliferation in the kidney, thus mediating AKI and ensuing fibrosis (47); knockout of the neutrophil chemoattractant Cxcl1 has been described to ameliorate cisplatin-induced AKI (48) and Icam1 deficiency has been shown to be protective in IRI (49). This underlines the importance of late injured *Vcam1*$^+$/*Ccl2*$^+$ PTCs in kidney disease progression.

A secondary validation of predictions from the snRNA-seq analysis by RNAscope in situ hybridization and immunofluorescence analysis confirmed the coexpression of *Ccl2* and *Nfkb1* as well as the expression of *Dock10* and *Il34* in injured Krt20$^+$, Vcam1$^+$ PTCs (Fig. 5 *A*–*E*). Approximately 17% of *GFP*$^+$ cells were positive for *Ccl2*, *Nfkb1*, and Vcam1, while no cells expressed all four markers in control kidneys (Fig. 5*D*). Quantification of the percentage of *Ccl2*, *Nfkb1*, and Vcam1-copositive cells among *Krt20*$^+$ cells showed similar results (*SI Appendix*, Fig. S4 *C* and *D*). Furthermore, Nfkb1-expressing PTCs were spatially associated with Cd45$^+$ immune cells, consolidating the role of these cells in persistent renal inflammation weeks after AKI (Fig. 5*F*).

To examine the human relevance of data from the moderate mouse AKI model, we assessed the expression of genes characteristic of *Vcam1*$^+$/*Ccl2*$^+$ cells in a previously published bulk RNA-seq dataset from human kidney transplant biopsies (7). This analysis delineated two distinct transcriptional trajectories in response to human AKI (7): successful repair [1] or disease progression via a transition state [2] to chronic injury [3]. Expression of *Vcam1*, *Ccl2*, *Nfkb1*, and *Dock10* were all significantly elevated in kidneys in the chronically injured state (Fig. 5*G*), further supporting the relevance of *Vcam1*$^+$/*Ccl2*$^+$ PTCs in the AKI-to-CKD transition.

Consistent with a prediction of up-regulated AP-1 regulon activity (Fig. 2*E*), expression of several AP-1 family members was increased in cluster 11 cells (Dataset S1). AP-1 also acts as a proinflammatory effector of both the TNF and the AGE/RAGE signaling pathways and has been implicated in development of organ fibrosis (50, 51). In addition, expression of genes linked to TGF-β signaling and kidney fibrosis like *Tgfb2*, *Tgfbr2*, *Smad1-3*, *Col4a1*, and *Col4a2* was enriched in late injured cells. Intriguingly, prosurvival (*Birc2*, *Birc3*, *Traf1*/*2*) as well as proapoptotic (*Fas*, *Casp4*, *Apaf1*, *Pmaip1*) target genes of both NF-κB and p53-mediated signaling were up-regulated in late injured cluster 11 cells (Fig. 4*C* and Dataset S1). Thus, proapoptotic gene activity may be countered by prosurvival networks maintaining dysfunctional epithelial cells within the nephron weeks after AKI.

Previous studies of long-term injury responses following IRI and other forms of AKI have pointed to PTCs arrested in the G_2/M phase of the cell cycle as a trigger of post-AKI fibrosis (12, 13). To examine the cell cycle state of PTCs in this study, we performed gene set enrichment analysis using diagnostic cell cycle gene sets (52, 53). Enrichment of all gene sets indicated the presence of cycling cells in the cycling early injured cluster. However, no enrichment of G_2/M phase gene sets could be detected in late injured cells (Fig. 4*D*). Cell cycle analysis using the *CellCycleScoring* function in Seurat to assign a S-phase or a G_2/M-phase score to every single cell in the dataset yielded the same result (*SI Appendix*, Fig. S4*B*). In accordance, immunofluorescence staining with phosphorylated histone 3 at serine 10 (p-H3), a G_2/M-phase marker (13), showed that <0.5% of all Vcam1$^+$ cells on day 28 post-IRI expressed p-H3 (*SI Appendix*, Fig. S4 *F* and *G*). These cells were predominantly located in the cortex (*SI Appendix*, Fig. S4*H*). The *Vcam1*$^+$/*Ccl2*$^+$ cells in the late injured cluster 11, however, comprised 6% of all *Vcam1*$^+$ cells in the IRI_d28 samples of the snRNA-seq dataset. Together, these data argue against a G_2/M phase arrested cell state in the majority of *Vcam1*$^+$/*Ccl2*$^+$ injured PTCs in this moderate injury model.

Analyses of age-related organ deterioration and tissue fibrosis have suggested that chronically senescent cells with a shared senescence-associated secretory phenotype (SASP) are involved in the development of tissue inflammation and fibrosis in many organ systems (54–57). Since the phenotype of a senescent cell is dynamic and heterogeneous depending on the type of senescence inducer, and on the cell and tissue type, we compared our data with transcriptomic signatures characteristic of the aging kidney and senescent cells and/or SASP, in various cell types subjected to different methods of senescence induction (Fig. 4*E*) (58–64). The "senescence core signatures" identified by Hernandez-Segura et al. (62) in fibroblasts, keratinocytes, melanocytes and astrocytes and by Casella et al. (63) in fibroblasts and endothelial cells were not enriched in late injured cells. Furthermore, the top 20 genes up-regulated in aging mouse kidneys by single-cell RNA-seq showed no enrichment in any of the clusters (58). However, a list of genes with a concordant increase in mRNA and protein level in the aging kidney (59) showed significant enrichment in three out of five IRI clusters, including cluster 11. Likewise, genes encoding proteins recently shown to be increasingly secreted by renal cortical epithelial cells upon irradiation induced senescence (64) and other SASP gene sets were significantly overrepresented in cluster 11 late injured cells.

To determine whether late injured cells arise from cells initiating replication in response to the primary IRI, we used a *Ki67*$^{Cre/ERT2}$ mouse line (65) crossed to INTACT mice and induced labeling with tamoxifen injection either on days 2 and 3 or on days 5 and 6 post-IRI. Following GFP labeling of replicating cells on days 2 and 3 post-IRI to the kidney at day 28 showed that 89% of Vcam1$^+$/*Ccl2*$^+$ cells at the CMB were GFP$^+$ (Fig. 6 *A* and *B*). In contrast, only 27% of Vcam1$^+$/*Ccl2*$^+$ cells in the cortex were GFP$^+$ at the day 28 time point. These observations lead to several conclusions. Cells with cluster 11 characteristics are evident at the site of primary injury in the hypersensitive S3 proximal tubule segments. Cells here initiated injury-invoked replication but failed to regenerate a normal PTC phenotype. In addition, cells with an indistinguishable molecular profile in cortical S1 and S2 segments reflect injury sites not associated with early injury-invoked proliferative repair. Furthermore, no cortical increase was observed in replicating cells among the Vcam1$^+$/*Ccl2*$^+$ population at 28 d when replicating cells were labeled at 5 and 6 d post-IRI (Fig. 6*B*). Thus, most cortical Vcam1$^+$/*Ccl2*$^+$ cells either originate from cells that were injured during the initial IRI, but did not initiate replication or show obvious injury responses at this time, or from a secondary spread of the injury within the CMB to the cortex. The observed spatial shift of the predominant location of Krt20-INTACT GFP positive cells from the CMB on day 7 to the cortex on day 28 post-IRI (Fig. 1*E* and *SI Appendix*, Fig. S1 *D* and *F*) supports the latter hypothesis.

The extent of renal injury and repair in the absence of an extrinsic trigger of AKI is an open question. Interestingly, a small number of control cells coclustered with injured PTCs (Fig. 2*C* and *SI Appendix*, Fig. S2*A*). Consistent with this finding, *Krt20*$^{T2A\text{-}CE}$ labeling identified rare Krt20$^+$/Vcam1$^+$ PTCs in healthy mouse kidneys (age: 3 mo; *SI Appendix*, Fig. S5). Some of the identified Vcam1$^+$ PTCs were Relb$^+$, and transcribed *Il34* and *Dock10*, indicating activation of the NF-κB signaling pathway in these cells, as in cell populations enriched in IRI (*SI Appendix*, Fig. S5). Rare Vcam1$^+$ and Vcam1$^+$/Havcr1$^+$ PTCs have also been identified in

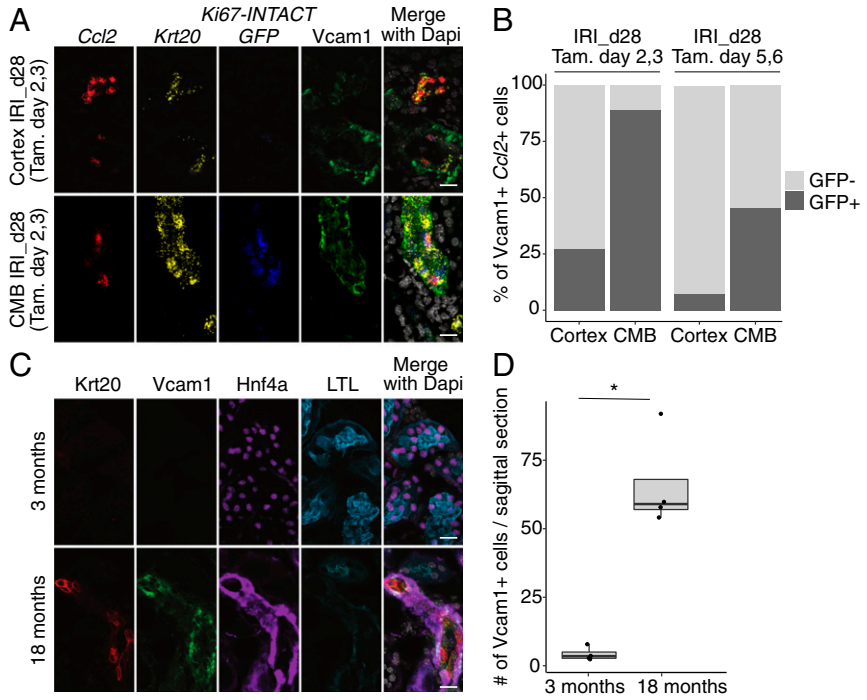

Fig. 6. The temporal and spatial relationship of PTC injury signatures in the mouse kidney. Lineage tracing of proliferating cells using a *Ki67*^{CreIERT2};INTACT mouse line with tamoxifen (Tam.) injections either on day 2 and 3 or on day 5 and 6 post-IRI. (*A*) RNAscope in situ hybridization (*Ccl2*, *Krt20*, *GFP*) combined with immunofluorescence staining (Vcam1) shows colocalization of *Ki67-INTACT GFP*-positive cells with Vcam1, *Krt20*, and *Ccl2* on day 28 post-IRI when tamoxifen is injected on day 2 and 3 post-IRI. (*B*) Quantification of *GFP* reporter in *Ccl2*$^{+}$/Vcam1^{+} cells in the cortex and the cortico-medullary boundary (CMB) at day 28 post-IRI in mice injected with tamoxifen either on day 2 and 3 ($n = 4$) or on day 5 and 6 ($n = 3$) post-IRI. (*C*) Immunofluorescence staining of proximal tubules with Krt20, Vcam1, Hnf4a, and LTL and quantification (*D*) of Vcam1^{+} PTCs in uninjured kidneys of 3- and 18-mo-old C57BL/6N mice. The gray box corresponds to the middle 50th percentile, the horizontal line to the median, and the whiskers indicate the 1.5 interquartile range. *$P < 0.05$. (Scale bar: *A* and *C*, 20 μm.)

normal adult human kidney samples (24, 66). These data suggest rare sporadic injury responses in the mouse and human kidney may mirror those initiated broadly in PTCs following IRI. These rare events are likely to increase with age. Consistent with this prediction, when Vcam1^{+} PTCs were scored in healthy 3- and 18-mo-old C57BL/6N mice, a marked increase of Vcam1^{+} PTCs was observed with age (Fig. 6 *C* and *D*).

Conclusions

PTCs play a major role in the regeneration of kidney structure and function following AKI (9). Our study provides high-resolution profiling of diverse injured PTC states, highlighting a role for NF-κB and AP-1 pathway activity in PTCs, and suggesting these regulatory pathways may drive PTCs to a pathological state. Of particular significance, we identified a *Vcam1*$^{+}$/*Ccl2*$^{+}$, proinflammatory, profibrotic PTC population, with a SASP that is shared with other organ systems (60–62).

Lineage tracing experiments suggest *Ccl2*$^{+}$ PTCs originate from failed repair of cells that initiated replication in response to the initial IRI insult, as hypothesized in a recent study (21), as well as from secondary injury sites within the cortex. Limited replicative labeling studies suggest secondary injury may not associate with cell death induced replicative repair, although additional studies are required for a definitive insight. Intriguingly, *Ccl2* has been shown to induce activation of NF-κB and AP-1 signaling as well as IL6 and ICAM1 expression in PTCs in vitro (67), and senescent cells are known to induce senescence in neighboring cells by paracrine signaling (68). Thus, autocrine and paracrine signaling by *Ccl2*$^{+}$ PTCs may contribute to the persistence of *Ccl2*$^{+}$ PTCs weeks after injury.

Previous studies have described G_2/M phase arrest as a characteristic of maladaptive PTCs after AKI (13). However, in our moderate injury model, neither snRNA-seq analysis nor immunolocalization of p-H3^{+} cells identified G_2/M arrest in direct injury-invoked or secondary injury-associated *Vcam1*$^{+}$ cells. In fate-mapping experiments, only a minor fraction of cortical *Vcam1*$^{+}$/*Ccl2*$^{+}$ cells showed a history of injury-invoked replication, which further supported the absence of G_2/M arrest in the majority of these cells. Additionally, a recent snRNA-seq study in a more severe IRI model (21) showed similar qualitative response features to the injury responses reported here. Thus, G_2/M arrest may not be a cell-intrinsic feature of proinflammatory PTCs remaining after kidney function is restored following AKI.

Senescent cells have emerged as important players in age-related kidney fibrosis and various kidney diseases (54, 68–70), and NF-κB signaling has been identified as a SASP activator (71). Our data demonstrate that *Vcam1*$^{+}$/*Ccl2*$^{+}$ PTCs share features with senescent cells including expression of *Plaur* encoding the urokinase-type plasminogen activator receptor (uPar). The improved outcome from successful removal of uPar^{+} cells through chimeric antigen receptor (CAR) T cell therapy in a liver fibrosis model (57), suggests a possible experimental route to blocking CKD progression following AKI.

Interestingly, *Vcam1*$^{+}$/*Ccl2*$^{+}$ cells exhibit an unusual mixed proapoptotic and antiapoptotic phenotype. As observed with cancer cells, despite the abnormal organization and cellular profile, antiapoptotic activities may promote survival of maladaptive PTCs that fail to complete renal repair. Targeting cell-intrinsic antiapoptotic pathways could be an alternative strategy to eliminate *Vcam1*$^{+}$/*Ccl2*$^{+}$ cells and determine whether their removal prevents progression to CKD.

Materials and Methods

See *SI Appendix* for a detailed description of materials and methods.

Mice, Surgical Procedures, and Serum Analysis. Mouse husbandry, handling, and surgical procedures were performed according to Institutional Animal Care and Use Committee guidelines at the University of Southern California (protocol numbers 11911 and 20894). IRI experiments were carried out on adult male mice (age, 11–19 wk; weight, 24–30 g) as in ref. 5, with a clamping time of 18 min to achieve a moderate injury level (no mortality until day 28 post-IRI). For sham surgery, the same procedure was performed except for clamping of the renal pedicles. Serum was collected for creatinine and/or BUN analysis at 48 h post-IRI and at collection.

Tissue Collection, Immunofluorescence, RNAscope in Situ Hybridization, and Image Analysis. Tissues were collected after organ perfusion with ice-cold DPBS (HyClone). Tissue sections were prepared and immunofluorescence staining performed as previously described (5). For RNAscope experiments, frozen sections were postfixed for 1–2 h in 4% PFA at 4 °C and then followed the manufacturer's protocol (ACD 323100-USM) for fixed-frozen tissues using TSA Plus fluorophores (Life Technologies). Dataset S5 lists used antibodies and probes. Images were acquired by confocal microscopy and quantified in randomly selected regions of interest or in sagittal sections as indicated ($n \geq 2$ for all image analyses) using Fiji (72). Datasets were compared by two-sided Student's *t* test or two-sided Wilcoxon test depending on their distribution. $P < 0.05$ was considered significant.

Nuclei Isolation and FACS Sorting. Nuclei were isolated from flash-frozen tissues with lysis buffer, Dounce homogenization, and filtering as in ref. 25 and resuspended in 1% BSA–DPBS supplemented with RNase inhibitor and Hoechst 33342. Hoechst$^+$, GFP$^+$ singlets were FACS sorted into a BSA–DPBS RNase inhibitor solution.

Single-Nucleus RNA-Seq. Nine samples were processed for snRNA-seq: two *Krt20$^{T2A\text{-}CE}$*;INTACT kidneys collected on day 7 after IRI, three *Krt20$^{T2A\text{-}CE}$*;INTACT kidneys collected on day 28 after IRI, and four control kidneys. FACS-sorted GFP$^+$ nuclei were counted and processed according to the 10× Chromium Single Cell 3′ protocol (v2 or v3). 10× libraries were sequenced using an Illumina NextSeq 500/550 High Output Kit v2. Alignment of sequencing reads was performed with the Cell Ranger Single-Cell Software Suite 3.0 (10× Genomics) using STAR aligner (73) on the University of Southern California High Performance Cluster. Filtered gene-cell expression matrices, removing cell barcodes not represented in nuclei, were created with the cellranger count function.

snRNA-Seq Data Analysis. The R packages Seurat v.3.2.2 (18), ggplot2 v.3.3.2, Matrix v.2.3-18, and dplyr v.1.0.2 were used for preprocessing, data analysis, and visualization in R Studio (R version 3.6.3). Seurat was used to filter out genes expressed in less than three nuclei and nuclei with low-quality profiles. Data were normalized and scaled using SCTransform (74) and integrated using integration anchors as described in ref. 18. The number of useful principal components (PCs) was determined using the ElbowPlot function and graph-based clustering performed. Differential gene expression analysis was performed on individual clusters. The subset function was employed to create a new Seurat-object comprising only PTC clusters, on which PC analysis, reclustering, and differential gene expression analysis were performed.

Gene modules were identified using the R package Monocle3 v.0.2.3.0 (75), GO and KEGG pathway enrichment analysis was performed using ClusterProfiler v.3.14.3 (76) and KEGG pathways visualized with GOplot v.1.0.2 (77). Fisher's exact test with Benjamini–Hochberg correction for multiple testing was employed for gene set enrichment analysis of published cell cycle and senescence gene sets (Dataset S4). The R package SCENIC v.1.1.2-2 was used to perform gene regulatory network analysis on IRI nuclei across all PTC clusters as previously described (31). The expression matrix generated with the SCTransform function in Seurat was used as input.

Analysis of Published Bulk RNA-Seq Dataset. Data were adopted from ref. 7. Samples were assigned to groups 1 (successfully repaired), 2 (transition), and 3 (chronically injured) according to the pseudotime analysis performed in ref. 7 (see ref. 7, figures 3C and 4A for pseudotime analysis). Groups were compared by Mann–Whitney *U* test. Box plots were generated using Prism 9.

Data Availability. The single-nuclei RNA sequencing data have been deposited in the Gene Expression Omnibus (GEO) database (accession no. GSE171417). All study data are included in the article and/or supporting information. Previously published data were used for this work (https://doi.org/10.1172/jci.insight.123151; https://doi.org/10.1038/s42255-020-0238-1).

ACKNOWLEDGMENTS. We thank Dr. Jordi van Gestel and Dr. Andrew Ransick for help with the bioinformatics analysis. L.M.S.G. was supported by the German Research Foundation with a postdoctoral scholarship (GE 3179/1-1). P.E.C. was supported by the Swiss National Science Foundation (Grant 167773), by the Gianella Foundation, and by the Balli Foundation. Work in A.P.M.'s laboratory was supported by a ReBuilding The Kidney Partnership grant from the National Institute of Diabetes and Digestive and Kidney Diseases (U01DK107350) and by a ReBuilding The Kidney Program grant (UC2DK126024).

1. R. L. Mehta *et al.*, International Society of Nephrology's 0by25 initiative for acute kidney injury (zero preventable deaths by 2025): A human rights case for nephrology. *Lancet* **385**, 2616–2643 (2015).
2. D. A. Ferenbach, J. V. Bonventre, Mechanisms of maladaptive repair after AKI leading to accelerated kidney ageing and CKD. *Nat. Rev. Nephrol.* **11**, 264–276 (2015).
3. G. M. Chertow, E. Burdick, M. Honour, J. V. Bonventre, D. W. Bates, Acute kidney injury, mortality, length of stay, and costs in hospitalized patients. *J. Am. Soc. Nephrol.* **16**, 3365–3370 (2005).
4. B. Bikbov *et al.*; GBD Chronic Kidney Disease Collaboration, Global, regional, and national burden of chronic kidney disease, 1990–2017: A systematic analysis for the Global Burden of Disease Study 2017. *Lancet* **395**, 709–733 (2020).
5. J. Liu *et al.*, Molecular characterization of the transition from acute to chronic kidney injury following ischemia/reperfusion. *JCI Insight* **2**, e94716 (2017).
6. P. E. Cippà *et al.*, A late B lymphocyte action in dysfunctional tissue repair following kidney injury and transplantation. *Nat. Commun.* **10**, 1157 (2019).
7. P. E. Cippà *et al.*, Transcriptional trajectories of human kidney injury progression. *JCI Insight* **3**, e123151 (2018).
8. M. Chang-Panesso, B. D. Humphreys, Cellular plasticity in kidney injury and repair. *Nat. Rev. Nephrol.* **13**, 39–46 (2017).
9. A. Zuk, J. V. Bonventre, Acute kidney injury. *Annu. Rev. Med.* **67**, 293–307 (2016).
10. J. V. Bonventre, Dedifferentiation and proliferation of surviving epithelial cells in acute renal failure. *J. Am. Soc. Nephrol.* **14**, S55–S61 (2003).
11. J.-K. Guo, L. G. Cantley, Cellular maintenance and repair of the kidney. *Annu. Rev. Physiol.* **72**, 357–376 (2010).
12. G. Canaud, J. V. Bonventre, Cell cycle arrest and the evolution of chronic kidney disease from acute kidney injury. *Nephrol. Dial. Transplant.* **30**, 575–583 (2015).
13. L. Yang, T. Y. Besschetnova, C. R. Brooks, J. V. Shah, J. V. Bonventre, Epithelial cell cycle arrest in G_2/M mediates kidney fibrosis after injury. *Nat. Med.* **16**, 535–543, 1p, 143 (2010).
14. A. Mo *et al.*, Epigenomic signatures of neuronal diversity in the mammalian brain. *Neuron* **86**, 1369–1384 (2015).
15. R. B. Deal, S. Henikoff, A simple method for gene expression and chromatin profiling of individual cell types within a tissue. *Dev. Cell* **18**, 1030–1040 (2010).
16. D. Legouis *et al.*, Altered proximal tubular cell glucose metabolism during acute kidney injury is associated with mortality. *Nat. Metab.* **2**, 732–743 (2020).
17. T. Ichimura *et al.*, Kidney injury molecule-1 (KIM-1), a putative epithelial cell adhesion molecule containing a novel immunoglobulin domain, is up-regulated in renal cells after injury. *J. Biol. Chem.* **273**, 4135–4142 (1998).
18. T. Stuart *et al.*, Comprehensive integration of single-cell data. *Cell* **177**, 1888–1902.e21 (2019).
19. S. S. Marable, E. Chung, J.-S. Park, Hnf4a is required for the development of Cdh6-expressing progenitors into proximal tubules in the mouse kidney. *J. Am. Soc. Nephrol.* **31**, 2543–2558 (2020).
20. S. Sasaki, A. Hara, M. Sakaguchi, M. Nangaku, Y. Inoue, Hepatocyte nuclear factor 4α regulates megalin expression in proximal tubular cells. *Biochem. Biophys. Rep.* **17**, 87–92 (2018).
21. Y. Kirita, H. Wu, K. Uchimura, P. C. Wilson, B. D. Humphreys, Cell profiling of mouse acute kidney injury reveals conserved cellular responses to injury. *Proc. Natl. Acad. Sci. U.S.A.* **117**, 15874–15883 (2020).
22. V. Rudman-Melnick *et al.*, Single-cell profiling of AKI in a murine model reveals novel transcriptional signatures, profibrotic phenotype, and epithelial-to-stromal crosstalk. *J. Am. Soc. Nephrol.* **31**, 2793–2814 (2020).
23. A. Ransick *et al.*, Single-cell profiling reveals sex, lineage, and regional diversity in the mouse kidney. *Dev. Cell* **51**, 399–413.e7 (2019).
24. D. Seron, J. S. Cameron, D. O. Haskard, Expression of VCAM-1 in the normal and diseased kidney. *Nephrol. Dial. Transplant.* **6**, 917–922 (1991).
25. H. Wu, Y. Kirita, E. L. Donnelly, B. D. Humphreys, Advantages of single-nucleus over single-cell RNA sequencing of adult kidney: Rare cell types and novel cell states revealed in fibrosis. *J. Am. Soc. Nephrol.* **30**, 23–32 (2019).
26. J. He, A. R. Green, Y. Li, S. Y. T. Chan, D.-X. Liu, SPAG5: An emerging oncogene. *Trends Cancer* **6**, 543–547 (2020).
27. J. Xu *et al.*, SPAG5-AS1 inhibited autophagy and aggravated apoptosis of podocytes via SPAG5/AKT/mTOR pathway. *Cell Prolif.* **53**, e12738 (2020).
28. B. R. Conway *et al.*, Association between variation in the actin-binding gene caldesmon and diabetic nephropathy in type 1 diabetes. *Diabetes* **53**, 1162–1165 (2004).
29. X. Liu, X. Li, Key genes involved in diabetic nephropathy investigated by microarray analysis. *J. Comput. Biol.* **26**, 1438–1447 (2019).

30. T. Ostendorf, F. Eitner, J. Floege, The PDGF family in renal fibrosis. *Pediatr. Nephrol.* **27**, 1041–1050 (2012).
31. S. Aibar *et al*., SCENIC: Single-cell regulatory network inference and clustering. *Nat. Methods* **14**, 1083–1086 (2017).
32. F. Massa *et al*., Hepatocyte nuclear factor 1β controls nephron tubular development. *Development* **140**, 886–896 (2013).
33. J. Li, J. Labbadia, R. I. Morimoto, Rethinking HSF1 in stress, development, and organismal health. *Trends Cell Biol.* **27**, 895–905 (2017).
34. A. Antonova *et al*., Heat-shock protein 90 controls the expression of cell-cycle genes by stabilizing Metazoan-specific host-cell factor HCFC1. *Cell Rep.* **29**, 1645–1659.e9 (2019).
35. F.-X. Yu, B. Zhao, K.-L. Guan, Hippo pathway in organ size control, tissue homeostasis, and cancer. *Cell* **163**, 811–828 (2015).
36. C.-L. Kim, S.-H. Choi, J.-S. Mo, Role of the Hippo pathway in fibrosis and cancer. *Cells* **8**, 468 (2019).
37. Y. Wang *et al*.; Cancer Genome Atlas Research Network, Comprehensive molecular characterization of the Hippo signaling pathway in cancer. *Cell Rep.* **25**, 1304–1317.e5 (2018).
38. S. Hao *et al*., NFAT5 is protective against ischemic acute kidney injury. *Hypertension* **63**, e46–e52 (2014).
39. Z. Ji, L. He, A. Regev, K. Struhl, Inflammatory regulatory network mediated by the joint action of NF-kB, STAT3, and AP-1 factors is involved in many human cancers. *Proc. Natl. Acad. Sci. U.S.A.* **116**, 9453–9462 (2019).
40. X.-M. Meng, D. J. Nikolic-Paterson, H. Y. Lan, TGF-β: The master regulator of fibrosis. *Nat. Rev. Nephrol.* **12**, 325–338 (2016).
41. T. Hayashida, M. Decaestecker, H. W. Schnaper, Cross-talk between ERK MAP kinase and Smad signaling pathways enhances TGF-β-dependent responses in human mesangial cells. *FASEB J.* **17**, 1576–1578 (2003).
42. M. Werth *et al*., Transcription factor TFCP2L1 patterns cells in the mouse kidney collecting ducts. *eLife* **6**, e24265 (2017).
43. D. Xu *et al*., c-Myc promotes tubular cell apoptosis in ischemia-reperfusion-induced renal injury by negatively regulating c-FLIP and enhancing FasL/Fas-mediated apoptosis pathway. *Acta Pharmacol. Sin.* **40**, 1058–1066 (2019).
44. G. Gadea, V. Sanz-Moreno, A. Self, A. Godi, C. J. Marshall, DOCK10-mediated Cdc42 activation is necessary for amoeboid invasion of melanoma cells. *Curr. Biol.* **18**, 1456–1465 (2008).
45. M. S. Hayden, S. Ghosh, Regulation of NF-κB by TNF family cytokines. *Semin. Immunol.* **26**, 253–266 (2014).
46. Y. Yamamoto *et al*., Development and prevention of advanced diabetic nephropathy in RAGE-overexpressing mice. *J. Clin. Invest.* **108**, 261–268 (2001).
47. J.-H. Baek *et al*., IL-34 mediates acute kidney injury and worsens subsequent chronic kidney disease. *J. Clin. Invest.* **125**, 3198–3214 (2015).
48. P. Liu, X. Li, W. Lv, Z. Xu, Inhibition of CXCL1-CXCR2 axis ameliorates cisplatin-induced acute kidney injury by mediating inflammatory response. *Biomed. Pharmacother.* **122**, 109693 (2020).
49. K. J. Kelly *et al*., Intercellular adhesion molecule-1-deficient mice are protected against ischemic renal injury. *J. Clin. Invest.* **97**, 1056–1063 (1996).
50. N. Nakagawa, *et al*., Pentraxin-2 suppresses c-Jun/AP-1 signaling to inhibit progressive fibrotic disease. *JCI Insight* **1**, e87446 (2016).
51. R. Eferl *et al*., Development of pulmonary fibrosis through a pathway involving the transcription factor Fra-2/AP-1. *Proc. Natl. Acad. Sci. U.S.A.* **105**, 10525–10530 (2008).
52. I. Tirosh *et al*., Dissecting the multicellular ecosystem of metastatic melanoma by single-cell RNA-seq. *Science* **352**, 189–196 (2016).
53. E. Z. Macosko *et al*., Highly parallel genome-wide expression profiling of individual cells using nanoliter droplets. *Cell* **161**, 1202–1214 (2015).
54. H. Jin *et al*., Epithelial innate immunity mediates tubular cell senescence after kidney injury. *JCI Insight* **4**, e125490 (2019).
55. S. Ferreira-Gonzalez *et al*., Paracrine cellular senescence exacerbates biliary injury and impairs regeneration. *Nat. Commun.* **9**, 1020 (2018).
56. M. Hashimoto *et al*., Elimination of $p19^{ARF}$-expressing cells enhances pulmonary function in mice. *JCI Insight* **1**, e87732 (2016).
57. C. Amor *et al*., Senolytic CAR T cells reverse senescence-associated pathologies. *Nature* **583**, 127–132 (2020).
58. Tabula Muris Consortium, A single-cell transcriptomic atlas characterizes ageing tissues in the mouse. *Nature* **583**, 590–595 (2020).
59. Y. Takemon *et al*., Proteomic and transcriptomic profiling reveal different aspects of aging in the kidney. *eLife* **10**, e62585 (2021).
60. M. Ruscetti *et al*., NK cell-mediated cytotoxicity contributes to tumor control by a cytostatic drug combination. *Science* **362**, 1416–1422 (2018).
61. R. I. Martínez-Zamudio *et al*., AP-1 imprints a reversible transcriptional programme of senescent cells. *Nat. Cell Biol.* **22**, 842–855 (2020).
62. A. Hernandez-Segura *et al*., Unmasking transcriptional heterogeneity in senescent cells. *Curr. Biol.* **27**, 2652–2660.e4 (2017).
63. G. Casella *et al*., Transcriptome signature of cellular senescence. *Nucleic Acids Res.* **47**, 7294–7305 (2019).
64. N. Basisty *et al*., A proteomic atlas of senescence-associated secretomes for aging biomarker development. *PLoS Biol.* **18**, e3000599 (2020).
65. O. Basak *et al*., Troy+ brain stem cells cycle through quiescence and regulate their number by sensing niche occupancy. *Proc. Natl. Acad. Sci. U.S.A.* **115**, E610–E619 (2018).
66. Y. Muto *et al*., Single cell transcriptional and chromatin accessibility profiling redefine cellular heterogeneity in the adult human kidney. *Nat. Commun.* **12**, 2190 (2021).
67. C. Viedt *et al*., MCP-1 induces inflammatory activation of human tubular epithelial cells: Involvement of the transcription factors, nuclear factor-kappaB and activating protein-1. *J. Am. Soc. Nephrol.* **13**, 1534–1547 (2002).
68. M. H. Docherty, D. P. Baird, J. Hughes, D. A. Ferenbach, Cellular senescence and senotherapies in the kidney: Current evidence and future directions. *Front. Pharmacol.* **11**, 755 (2020).
69. D. J. Baker *et al*., Naturally occurring p16(Ink4a)-positive cells shorten healthy lifespan. *Nature* **530**, 184–189 (2016).
70. J. Liu *et al*., Accelerated senescence of renal tubular epithelial cells is associated with disease progression of patients with immunoglobulin A (IgA) nephropathy. *Transl. Res.* **159**, 454–463 (2012).
71. A. Salminen, A. Kauppinen, K. Kaarniranta, Emerging role of NF-κB signaling in the induction of senescence-associated secretory phenotype (SASP). *Cell. Signal.* **24**, 835–845 (2012).
72. J. Schindelin *et al*., Fiji: An open-source platform for biological-image analysis. *Nat. Methods* **9**, 676–682 (2012).
73. A. Dobin *et al*., STAR: Ultrafast universal RNA-seq aligner. *Bioinformatics* **29**, 15–21 (2013).
74. C. Hafemeister, R. Satija, Normalization and variance stabilization of single-cell RNA-seq data using regularized negative binomial regression. *Genome Biol.* **20**, 296 (2019).
75. J. Cao *et al*., The single-cell transcriptional landscape of mammalian organogenesis. *Nature* **566**, 496–502 (2019).
76. G. Yu, L.-G. Wang, Y. Han, Q.-Y. He, clusterProfiler: An R package for comparing biological themes among gene clusters. *OMICS* **16**, 284–287 (2012).
77. W. Walter, F. Sánchez-Cabo, M. Ricote, GOplot: An R package for visually combining expression data with functional analysis. *Bioinformatics* **31**, 2912–2914 (2015).